International Journal of Heat and Mass Transfer 228 (2024) 125678

Contents lists available at ScienceDirect

International Journal of Heat and Mass Transfer

journal homepage: www.elsevier.com/locate/ijhmt

Improving phase change heat transfer in an enclosure partially filled by uniform and anisotropic metal foam layers

Mohammad Ghalambaz [a,*], Mikhail Sheremet [a], Kyle Shank [b,c], Saeed Tiari [b], Mehdi Fteiti [d]

[a] Laboratory on Convective Heat and Mass Transfer, Tomsk State University, Tomsk 634050, Russia
[b] Biomedical, Industrial, and Systems Engineering Department, Gannon University, 109 University Square PA 16541, USA
[c] Mechanical Engineering Department, Gannon University, 109 University Square PA 16541, USA
[d] Physics Department, Faculty of Science, Umm Al-Qura University, Makkah 24381, Saudi Arabia

ARTICLE INFO

Keywords:
Anisotropic metal foams
Latent heat thermal energy storage (LHTES)
Phase change
Copper metal foam
Anisotropic metal foam layer (AMFL)

ABSTRACT

Anisotropic metal foams exhibit exceptional potential for improving the efficiency of latent heat thermal energy storage (LHTES) units by enhancing heat transfer and thermal energy storage rates. This study explores the largely uncharted area of thermal behavior of anisotropic metal foams in varied configurations and enclosure designs. The research focuses on an LHTES unit with a specific channel configuration, constructed using copper and containing three layers of copper metal foam, one of which is anisotropic and infused with paraffin wax. The finite element method was utilized to manage the complexities emerging from phase change, and the anisotropic angle varied from 0 to 90° in three different placements of the AMFL: top, middle, or bottom of the enclosure. The ideal design was achieved with an AMFL in the middle with a 0°angle, resulting in a 3.7 % reduction in melting time and approximately a 2.3 % reduction in solidification time. However, AMFL designs at the middle placement with a 75° anisotropic angle were less effective, hampering the melting and solidification processes, thus potentially extending charging and discharging times. The study concludes that the placement and angle of the AMFL layer are vital for the heat transfer capabilities of phase change materials. AMFL at the middle with a 0° angle optimally leverages temperature gradients, enhancing heat transfer compared to other investigated cases. An AMFL in the middle with a 0° angle exhibits approximately 7.1 % and 6.3 % improvements for melting fractions of 0.9 and 0.95, respectively, underscoring its potential for efficient thermal energy storage.

1. Introduction

Latent heat thermal energy storage (LHTES) is a promising technique for storing thermal energy as latent heat during the phase transition of a material [1]. Phase change materials (PCMs) are employed within LHTES units due to significant latent heat energy storage density and may absorb or release a considerable quantity of thermal energy throughout phase transition while experiencing an isothermal process [2]. The heat absorbed or released during phase transition is known as latent heat. LHTES systems may be used for several purposes, including but not limited to buildings [3,4] and waste heat recovery [5]. LHTES systems may lower heating and cooling energy consumption for buildings. In the summer, LHTES systems may collect excess building heat during the day and release it to the ambient at night to cool the building, while in the winter, they can absorb the ambient heat during the day and release it to the structure at night [6,7]. This assists in transferring energy usage from peak to off-peak hours, reducing pressure on the power system and lowering energy expenditures.

Another possible use for LHTES systems is waste heat recovery. In industrial operations, a significant quantity of waste heat is produced that may be recovered to create heat or power. LHTES devices may be deployed to store waste heat and release it when required, enhancing overall energy efficiency [5,8]. There are many applications that require a wide range of operating temperatures, and the PCMs can be designed accordingly. Thus, various types of PCMs have been synthesized and developed. PCMs are classified under two major categories for use in LHTES systems: organic and inorganic. Organic PCMs mainly consist of paraffin or fatty acids [4], while inorganic PCMs include but are not limited to salt hydrates and metals [9]. The chosen PCM is dependent on the application and operating temperature range required. LHTES systems are generally comprised of a container or vessel containing the PCM and a heat exchanger for transferring heat to or from the PCM [10,

* Corresponding author.
E-mail address: m.ghalambaz@gmail.com (M. Ghalambaz).

https://doi.org/10.1016/j.ijheatmasstransfer.2024.125678
Received 22 June 2023; Received in revised form 26 April 2024; Accepted 5 May 2024
Available online 11 May 2024

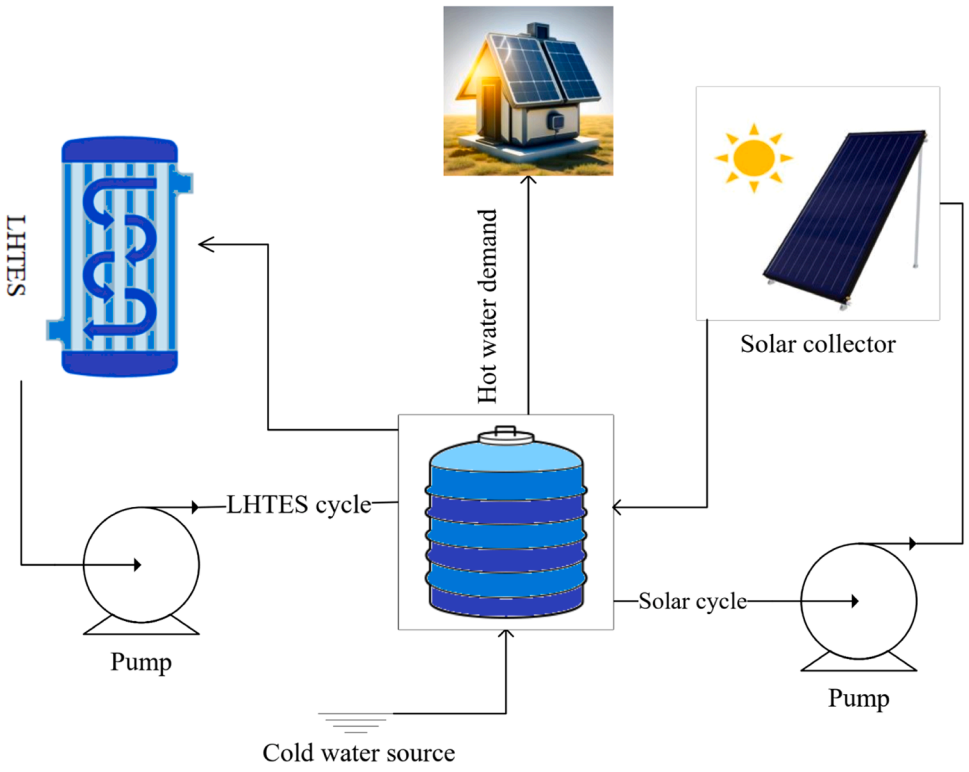

Fig. 1. An illustration of a solar heating system designed for heating buildings. The system comprises several components: a solar collector, water storage tank, LHTES unit, and circulating pumps.

11]. Metal foams may enhance the heat transfer performance of LHTES systems by expanding the heat transfer's effective surface area and improving the effective thermal conductivity of metal foam-PCM composites. LHTES systems and PCMs can greatly enhance energy efficiency and decrease energy costs in a broad scope of applications, from buildings to industrial operations. Further optimization of the thermal performance of these systems and widespread adoption of them will need continued research and development.

LHTES is essential to the development of solar energy technology since solar energy is a weather- and time-dependent intermittent energy source. An LHTES system is able to store a substantial quantity of thermal energy at fusion temperature in a small volume, hence minimizing energy fluxes in transitory solar energy systems. A solar heating system for building heating is presented in Fig. 1 as an illustration. The system is composed of a solar collector, water storage tank, LHTES unit, and circulating pumps. The collector heats water and stores it as sensible heat in the hot water tank, which provides on-demand hot water to the structure. An auxiliary cycle connects the hot water storage tank to the LHTES unit. When energy demand is low, or energy production is high, the pump in the auxiliary energy storage loop activates and transfers its excess heat to the LHTES unit. When solar energy generation is insufficient, the tank can also extract energy from the LHTES unit.

The poor thermal conductivity of PCMs has been a major drawback to their widespread use in LHTES systems; nevertheless, metal foam has recently emerged as a viable porous material to overcome this problem. The porous nature of metal foams is a promising candidate for improving the functionality of LHTES systems by facilitating heat transfer and thermal energy storage [12,13].

Accurate modeling of PCM embedded with metal foams is crucial in designing LHTES systems and may demand a local thermal non-equilibrium (LTNE) approach. LTNE is a significant occurrence in porous media. The existence of a porous matrix and linked fluid-filled holes in these materials results in a large variance in the temperature field. In LTNE, the temperature of the solid matrix and fluid are not equivalent, and their heat transfer is not in equilibrium [14,15]. This is because solid and liquid phases have differing thermal conductivities, resulting in temperature differences at the liquid-solid interface. In some instances, the LTNE phenomena might impair the thermal performance of metal foams; consequently, it is crucial to model and comprehend this phenomenon precisely. Numerical models and experimental investigations of the impacts of LTNE in porous media and metal foams have shown that the temperature gradient at the liquid-solid interface may substantially influence the overall heat transfer performance. Understanding the LTNE phenomena is essential for improving the design of heat exchangers and other engineering systems using porous media and metal foams [16].

Several studies employed local thermal equilibrium (LTE) and examined the phase change heat transfer of PCMs. For example, [17–20] explored using PCMs for energy storage and thermal control. These studies provide efficient ways to implement PCMs for thermal control and optimize energy storage capacities. Other studies also investigated phase change heat transfer aspects with the LTE approach [21]. To promote the accuracy of phase change heat transfer modeling in metal foams, some researchers have used the LTNE approach [19,22–29]. This approach incorporates heat transfer between the PCM inside the pores and the porous matrix into the governing equations through a coupling source term. The source term depends on the temperature difference between phases, the surface area of the pores connected to the PCM, and the convective heat transfer coefficient. A Nusselt number and pore geometrical feature are needed to calculate the convective heat transfer coefficient (h). Many studies have used the pore scale Reynolds number or Rayleigh (Grashof) number in the Nusselt number and convective heat transfer coefficient calculations [26,27]. However, the pore scale Rayleigh number cannot accurately represent the fluid velocity within the pores because the liquid PCM moves between a group of pores and is not limited to a single cell. Therefore, the Reynolds number, which is a function of overall fluid velocity, can better represent the fluid interaction with the pore surfaces. Some studies have used equations tailored

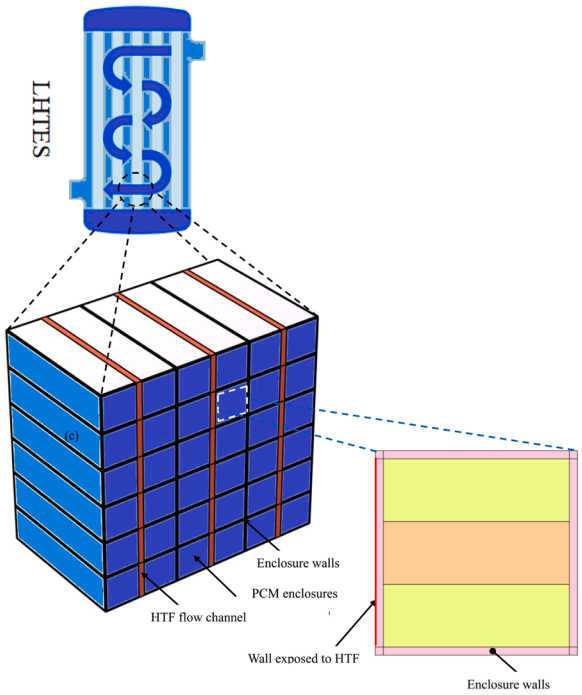

Fig. 2. A multi-channel LHTES unit and a 2D section of one of the storage enclosures.

for forced convection flows and high Reynolds numbers to represent the Nusselt number using the Reynolds number [19,22–25]. However, using such equations would result in a zero convective heat transfer coefficient when there is zero liquid/solid velocity. This is physically not feasible since there is always a conduction heat transfer mechanism between the solid matrix and the PCM inside the pores. Thus, the closure equations for computing the convective heat transfer coefficient should not provide zero values as non-zero values were computed in [20,28,29].

Previous literature used less accurate Nusselt number equations due to the lack of reliable equations. Recently, some literature has focused on providing closure models and relations for very low Reynolds numbers (of scale 1) that are suitable for natural convection flows of liquid PCMs in metal foam cells. Yao et al. [30] simulated the low Reynolds number convection heat transfer in the pore scale. They provided an adequate non-zero relation based on the Reynolds number for computation of the pore scale Nusselt number, which can be applied to LTNE modeling of LHTES for PCMs.

Researchers have examined partial layers of metal foams or numerous layers of metal foams with various porosities to reduce the cost and weight of metal foams while enhancing their heat transmission capabilities (known as gradient porosity). This method is gaining popularity because it permits a more focused and effective heat transfer solution without additional material. In [31], scientists proposed employing metal foams with graded morphologies to improve the performance of thermal energy storage using PCMs. Using the best configuration, the researchers saw a 3.35 % increase in charging time and a 7.96 % increase in overall entropy production. Liu et al. [32] developed a revolutionary tank design with graded metal foams to improve melting and solidification efficiency, resulting in a 21.1 % decrease in melting time and a 10.0 % reduction in the entire cycle. Examining the solidification behavior of PCMs enhanced with pin fins and metal foam with gradient pore parameters, Yang et al. [33] discovered that the optimal heat transfer structure is a hybrid of pin fins and gradient pore porosity metal foam. In [34], researchers aimed to improve the thermal performance of LHTES units with a novel construction that combines graded metal foam and fins. When contrasted with the graded metal foam structure, the novel configuration — characterized by a porosity gradient of 2 %, fin thickness of 3 mm, and a fin angle of 25° — notably enhances performance. Specifically, it elevates the rate of thermal energy storage by 36.52 % and decreases the total melting time by 27.23 %.

The application of anisotropic metal foam in latent heat thermal energy storage systems offers several advantages due to its unique material and flow characteristics. Open-cell metal foams are of particular interest for their high specific surface area and intricate tortuosity, which contribute to enhanced convective heat transfer capabilities [35]. Various numerical methods, including volume-averaging techniques and a local thermal non-equilibrium model, have been employed to assess heat transfer within these foams. The focus has been on understanding the impact of elongated foam cells, porosity levels, and fluid inlet velocities on interfacial heat transfer coefficients and Nusselt numbers [35]. Anisotropy in metal foams can influence flow characteristics significantly. A pore-scale numerical study examined the impact of skeleton micropores and anisotropic flow behavior within three-dimensional foam structures [36]. The results revealed that the pressure drop was highest in the Y-direction compared to the other axes, emphasizing the importance of accounting for anisotropic characteristics in actual metal foams. Metal foams have also been considered for their potential to enhance the properties of PCMs, which are commonly used in latent heat thermal energy storage but suffer from poor heat transfer rates [37]. Pore-scale simulations of metal foams with uniform and graded porosities have shown promising results, demonstrating accelerated melting times in structures with specific porosity gradients.

Recent studies have investigated the enhancement of heat transfer in LHTES units using metal foams, focusing on anisotropic and heterogeneous foams. The potential of combining anisotropic metal foams with phase change materials in a shell-tube storage unit was explored through computational modeling [38]. Utilizing finite element methods and artificial neural networks, the study found that adjusting the anisotropic angle could significantly optimize the energy storage rate, reducing melting time by around 7 % without affecting storage capacity. Anisotropic metal foams with engineered local properties, for instance, have been mathematically modeled and tested using the finite element method in a copper-coconut oil LHTES unit [39]. The foam's orientation or anisotropic and mounting tilt angles significantly impacted the thermal energy storage power and the phase transition behavior. Optimum tilt angles, combined with a 0° anisotropic angle, maximized charging power with up to 20 % reduction in charging time compared to regular metal foams [39].

In another study, a mathematical model was developed for heterogeneous metal foams embedded in a side wall heated cavity, where the thermal conductivity and permeability were defined by tensors [40]. The heterogeneity of the foam was manipulated by a heterogeneity parameter and angle. Findings showed that heat transfer was enhanced with increased heterogeneity, which reduced the melting time. Interestingly, the charging time was altered by up to 24 % for a heterogeneity parameter of 0.2, proving the heterogeneity provided a significant impact [40]. Compared to the simple foam with an equivalent weight, a heterogenous metal showed an 11 % reduction in charging time [40]. Both studies [39,40] highlighted the potential of these advanced foam designs for improving the performance of LHTES units without incurring penalties in weight or capacity.

Given that anisotropic metal foams have demonstrated their ability to enhance heat transfer and thermal energy storage rates in LHTES units without compromising weight or capacity, as per the literature review, they emerge as excellent prospects for incorporation in LH TES systems. However, existing studies on this subject are relatively sparse, and a comprehensive understanding of the thermal behavior of anisotropic metal foams across various configurations and enclosure designs remains a void in current knowledge. Therefore, this study is dedicated to pioneering an investigation into the influence of the placement and angle of an anisotropic metal foam layer infused with PCM, exploring the charging and discharging behavior of an LHTES unit.

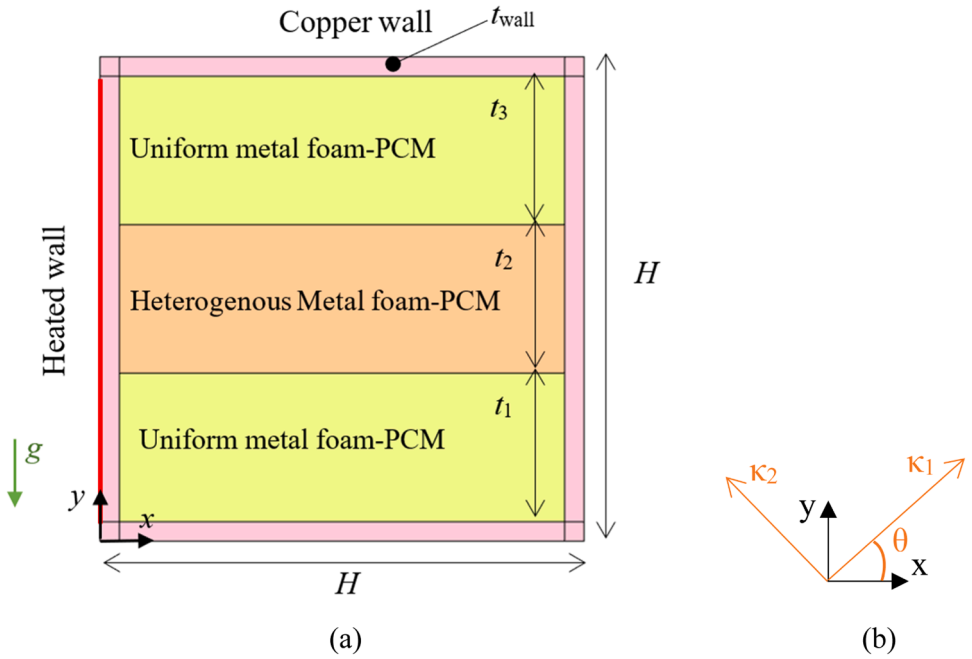

Fig. 3. Representation of the PCM enclosure as a 2D model containing a layer of anisotropic metal foam. (a) the enclosure details; (b) the definition of anisotropic angles.

2. Model description

The LHTES unit, presented in Fig. 2, is created utilizing a channel configuration. Water, used as the heat transfer fluid (HTF), is passed through the channels and thermally interacts with the PCM inside the enclosures. The channel walls are made of copper with a thickness of t_{wall}. The channels are stacked vertically, and there is a small gap between them in the vertical direction for maintenance and mechanical stability. The enclosure is filled by three layers of metal foams (MFs) of porosity ε. One of the layers is an anisotropic metal foam layer with an anisotropic angle θ. The metal foam (MF) layer is filled with paraffin wax and forms a composite metal foam-phase change material (MF-PCM), a phase transition substance that stores/releases latent heat energy at T_f. Depending on the discharging/charging procedure, water exchanges heat with the PCM domain via the channel wall and departs at a higher or lower temperature. Multiple LHTES units can be coupled in parallel, series, or a hybrid configuration to suit the capacity and demand requirements of Fig. 1's cycle. The objective is to investigate the design of an LHTES unit that includes a layer of anisotropic foam through a heat transfer approach.

The deficient heat conduction rate of PCMs is a key difficulty for LHTES units, as it can slow down the energy storage/release rate. Therefore, to boost the unit's heat transfer rate and response time, a layer of anisotropic foam was added. The cycle works between two temperatures of $T_h = T_f + 15°C$ and $T_c = T_f - 15°C$. When the LHTES unit has an initial temperature of $T_{initial} = T_c$, the hot tank dumps extra thermal energy into the LHTES unit at a set point temperature of T_h. Consequently, T_h is considered to be the HTF's inlet temperature, and $T_{initial} = T_c$ during the charging process. In contrast, during a discharging process, the hot tank takes energy from the fully charged LHTES ($T_{initial}=T_h$) while HTF temperature is T_c. The full charging and discharging processes are analyzed in the present study. Fig. 3 shows a view of the channel model with three layers of metal foams. The anisotropic metal foam layer can be placed in the bottom, middle, or top. Thus, the present study considers three cases of Anisotropic MF Layer (AMFL) at the Bottom, Middle, or Top for thermal energy storage investigation. Owing to the gap between the channels in the vertical direction, the top and bottom walls of the channels were assumed to be insulated.

2.1. Governing equations

The physical domain consists of three interconnected regions: the copper tube wall, clear PCM, and composite MF-PCM. The transient conduction heat transfer equation (Eq. (1)) represents the conduction the copper wall experiences. The density, specific heat capacity, and thermal conductivity of the wall are represented by ρ, Cp, and k, respectively. The temperature field and time are denoted by T and t, respectively, and the subscript wall applies to all properties and field variables. However, for convenience, this subscript has been removed.

$$(\rho C_p)\frac{\partial T}{\partial t} = k\left(\frac{\partial^2 T}{\partial x^2} + \frac{\partial^2 T}{\partial y^2}\right) \tag{1}$$

The PCM and metal foam domain are expressed by governing equations in a unified form, which is later tailored for each region by controlling permeability and porosity. The energy conversion equation uses the LTNE approach to account for heat transfer in each PCM and metal foam phase separately. Coupling source terms are used to consider energy transfer between phases. Free convection occurs in the molten PCM in both the open-cell foam and clear regions, so the mass conservation (continuity) and momentum equations are introduced in the PCM and PCM-MF regions. The phase change is simulated utilizing the enthalpy-porosity formulation, and to render zero velocity in the solid PCM, source terms are added to the momentum equations as a function of melt volume fraction (f). The Darcy-Brinkman-Forchheimer model is used to model fluid flow in the metal foam. Partial differential equations are employed for the governing equations of the conservation of mass, momentum, and energy as follows [41–43]:

Continuity:

$$\frac{\partial u}{\partial x} + \frac{\partial v}{\partial y} = 0 \tag{2}$$

Momentum:

$$\frac{\rho_{\mathrm{PCM}}}{\varepsilon}\frac{\partial u}{\partial t}+\frac{\rho_{\mathrm{PCM}}}{\varepsilon^2}\left(u\frac{\partial u}{\partial x}+v\frac{\partial u}{\partial y}\right)=-\left(\frac{\partial p}{\partial x}\right)+\frac{1}{\varepsilon}\left[\frac{\partial}{\partial x}\left(\mu_{\mathrm{PCM}}\frac{\partial u}{\partial x}\right)+\frac{\partial}{\partial y}\left(\mu_{\mathrm{PCM}}\frac{\partial u}{\partial y}\right)\right]-\frac{\mu_{\mathrm{PCM}}}{\kappa}u-\rho_{\mathrm{PCM}}\frac{C_F}{\sqrt{\kappa}}|U|u+A_{mush}\frac{(1-f(T))^2}{\lambda_{mush}+f^3(T)}u \tag{3a}$$

$$\frac{\rho_{\mathrm{PCM}}}{\varepsilon}\frac{\partial v}{\partial t}+\frac{\rho_{\mathrm{PCM}}}{\varepsilon^2}\left(u\frac{\partial v}{\partial x}+v\frac{\partial v}{\partial y}\right)=-\left(\frac{\partial p}{\partial y}\right)+\frac{1}{\varepsilon}\left[\frac{\partial}{\partial x}\left(\mu_{\mathrm{PCM}}\frac{\partial v}{\partial x}\right)+\frac{\partial}{\partial y}\left(\mu_{\mathrm{PCM}}\frac{\partial v}{\partial y}\right)\right]+g\rho_{\mathrm{PCM}}\beta_{\mathrm{PCM}}(T-T_0)-\frac{\mu_{\mathrm{PCM}}}{\kappa}v-\rho_{\mathrm{PCM}}\frac{C_F}{\sqrt{\kappa}}|U|v+A_{mush}\frac{(1-f(T))^2}{\lambda_{mush}+f^3(T)}u_z \tag{3b}$$

Energy conservation in the PCM phase:

$$\varepsilon(\rho C_p)_{\mathrm{PCM}}\frac{\partial T_{\mathrm{PCM}}}{\partial t}+(\rho C_p)_{\mathrm{PCM}}\left(u\frac{\partial T_{\mathrm{PCM}}}{\partial x}+v\frac{\partial T_{\mathrm{PCM}}}{\partial y}\right)=\frac{\partial}{\partial x}\left(k_{\mathrm{eff,PCM}}\frac{\partial T_{\mathrm{PCM}}}{\partial x}\right)+\frac{\partial}{\partial y}\left(k_{\mathrm{eff,PCM}}\frac{\partial T_{\mathrm{PCM}}}{\partial y}\right)+h_v(T_{\mathrm{MF}}-T_{\mathrm{PCM}})-\varepsilon\rho_{\mathrm{PCM}}L_{\mathrm{PCM}}\frac{\partial f(T)}{\partial t} \tag{4a}$$

Energy conservation in the MF phase:

$$(1-\varepsilon)(\rho C_p)_{\mathrm{MF}}\frac{\partial T_{\mathrm{MF}}}{\partial t}=\frac{\partial}{\partial x}\left(k_{\mathrm{eff,\,MF}}\frac{\partial T_{\mathrm{MF}}}{\partial x}\right)+\frac{\partial}{\partial y}\left(k_{\mathrm{eff,MF}}\frac{\partial T_{\mathrm{MF}}}{\partial y}\right)-h_v(T_{\mathrm{MF}}-T_{\mathrm{PCM}}) \tag{4b}$$

The coefficient of thermal volume expansion (β), the Frochheimer parameter (C_F), the latent heat of fusion (L), the porous permeability (κ), and the acceleration of gravity (g) are utilized in the above equations. Using the pore scale Nusselt number, the interstitial heat transfer coefficient in the volumetric form (h_v) is added subsequently in the model. The subscripts MF, PCM, and eff are used to signify, respectively, metal foam, PCMs, and effective properties.

Incorporating source terms comprising A_{mush} and λ_{mush} into the model forces the fluid velocity in solid zones to zero. In order to accomplish this, the model uses a considerable value of A_{mush} for clear flow (6×10^6 Pa.s/m^2) and metal foam region (1×10^{10} Pa.s/m^2) to dominate the flow solution in solid zones. In addition, the value of λ_{mush} is set to 0.001 to prevent the denominator from equaling zero in the source terms.

To maintain solver stability and constrain a zero velocity in solid zones, the dynamic viscosity as a function of f was employed. Specifically, the model defined the viscosity as $\mu=\mu_{\mathrm{PCM,l}}f+(1\text{-}f)\times a$, where a is an intentionally high value for viscosity (10^4 Pa.s). When f=1 in the formula, the viscosity approaches the normal dynamic viscosity of the $\mu_{\mathrm{PCM,l}}$ in the liquid area, and when f=0, it climbs to a significant value in the solid region, contributing to increasing flow resistance in solid areas.

The heat transport equations for the PCM and MF phases in the LTNE model are Eqs. (4a) and (4b), respectively. Thermal interaction between the two phases is represented by the term h_v (T_{MF}-T_{PCM}). In these equations [44], the PCM ($k_{\mathrm{eff,PCM}}$) and MF ($k_{\mathrm{eff,\,MF}}$) effective thermal conductivities are used to account for the influence of pore architectures on thermal conductivities. The melting volume fraction, f, is controlled by temperature as provided below [45]:

$$f(T)=\begin{cases}0 & T<T_{\mathrm{f}}-\frac{1}{2}\Delta T_{\mathrm{f}}\ (\text{Solid phase})\\ \frac{(T-T_{\mathrm{f}})}{\Delta T_{\mathrm{f}}}+\frac{1}{2} & T_{\mathrm{f}}-\frac{1}{2}\Delta T_{\mathrm{f}}\le T\le T_{\mathrm{f}}+\frac{1}{2}\Delta T_{\mathrm{f}}\ (\text{Mushy region})\\ 1 & T>T_{\mathrm{f}}+\frac{1}{2}\Delta T_{\mathrm{f}}\ (\text{Liquid phase})\end{cases} \tag{5}$$

For AMFL, the MF layer's thermal conductivity and permeability can vary in different directions. The MF ligaments are strengthened unidirectionally to improve heat conductivity at the price of permeability. Consequently, a tensor of second order is employed to represent them, as illustrated in the following equations [46]:

$$\kappa=\begin{bmatrix}\kappa_2(\sin\theta)^2+\kappa_1(\cos\theta)^2 & (\kappa_1-\kappa_2)(\cos\theta)(\sin\theta)\\ (\kappa_1-\kappa_2)(\cos\theta)(\sin\theta) & \kappa_2(\cos\theta)^2+\kappa_1(\sin\theta)^2\end{bmatrix} \tag{6}$$

$$k_{\mathrm{eff,\,MF}}=\begin{bmatrix}k_2(\sin\theta)^2+k_1(\cos\theta)^2 & (k_1-k_2)(\sin\theta)(\cos\theta)\\ (k_1-k_2)(\sin\theta)(\cos\theta) & k_2(\cos\theta)^2+k_1(\sin\theta)^2\end{bmatrix} \tag{7}$$

The aforementioned equations yield values k_1=(1+σ) × k_{m}, k_2=(1-σ) × k_{m}, and κ_1=(1-σ) × κ_m, κ_2=(1+σ) × κ_{m} where subscript m denotes the average property of MF. Fig. 2 defines the angle of the anisotropic arrangement of the MF in the enclosure. The anisotropic factor σ represents the amount of anisotropy in the thermal conductivity, and the permeability of the σ =0 is equivalent to an isotropic MF. In this study, a moderate value of σ =0.3 is selected since the anisotropic factor cannot be exceedingly high and must maintain the continuity of the MF. Based on prior research [41,44,47], the average permeability (κ_a) and effective thermal conductivity (k_a) of the MF are determined as:

$$k_a=\frac{1-\varepsilon}{3}k_{\mathrm{MF}} \tag{8a}$$

$$\kappa_a=\frac{\varepsilon^2\left(d_{fp}\sqrt{\frac{\kappa_{tor}}{3\varepsilon}}\right)^2}{36(\kappa_{tor}-1)\kappa_{tor}} \tag{8b}$$

Additional equations must be considered that introduce d_{fs} and tor. These equations define k_{MF}, the thermal conductivity of the MF material's bulk, and can be explained as [47]:

$$d_{fs}=1.18\sqrt{\frac{1-\varepsilon}{3\pi}}\left\{\frac{1}{1-e^{\frac{(\varepsilon-1)}{0.04}}}\right\}d_{fp} \tag{8c}$$

$$\frac{1}{\kappa_{tor}}=\frac{3}{4\varepsilon}+\frac{\sqrt{9-8\varepsilon}}{2\varepsilon}\cos\left\{\frac{4\pi}{3}+\frac{1}{3}\cos^{-1}\left(\frac{8\varepsilon^2-36\varepsilon+27}{(9-8\varepsilon)^{\frac{3}{2}}}\right)\right\}d_{fp} \tag{8d}$$

where pore per inch (PPI) property (d_{fp}) and Frochheimer parameter were evaluated as [47];

$$d_{fp}=\frac{0.0254}{PPI} \tag{8e}$$

$$C_F=0.00212(1-\varepsilon)^{-0.132}\left(\frac{d_{fs}}{d_{fp}}\right)^{-1.63} \tag{9}$$

The volumetric interstitial heat transfer coefficient was used to evaluate the heat exchange between the MF and PCM for low Reynolds numbers at the pore scale [30]:

$$h_v=Nu_v\frac{k_{\mathrm{PCM}}}{d_{fs}^2} \tag{10a}$$

Table 1
Material characteristics copper foam (MF) and paraffin (PCM).

Materials	C_p (J/kg.K)	ρ (kg/m^3)	k (W/m.K)
Paraffin (solid/liquid) [48–50]	2700/2900	916/790	0.21/0.12
Copper foam [51]	386	8900	380

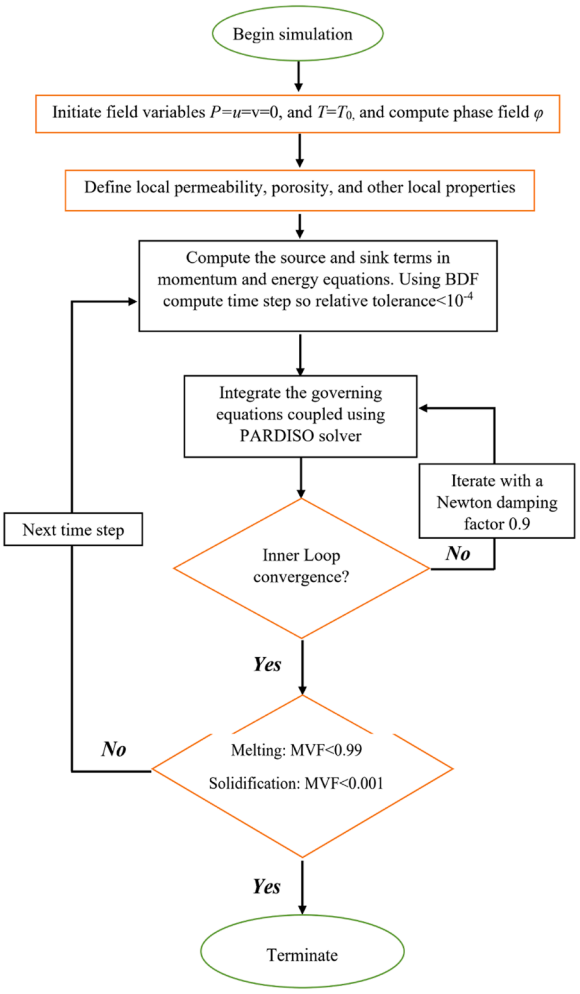

Fig. 4. Diagram of the numerical approach used for deciphering the governing equations.

Table 2
Mesh details for various values of mesh resolution parameter (m).

m	Quads	Edge elements	Computational time	
			Melting	Solidification
4	16384	1264	2 h 57 min	50 min
5	25600	1580	5 h 2 min	1 h 19 min
6	36864	1896	7 h 32 min	2 h 3 min
7	50176	2212	5 h 2 min	3 h 14 min

$$Nu_v = \begin{cases} 76.99 - 152.01\varepsilon + 75.04\varepsilon^2 & 0 \le \mathrm{Re} \le 0.1 \\ (1.72 + 1.71\varepsilon - 3.46\varepsilon^2)\mathrm{Re}^{0.26}\mathrm{Pr}^{0.28} & 0.1 < \mathrm{Re} \le 1 \end{cases} \quad (10b)$$

The symbols Pr, α, and Re indicate the dimensionless Prandtl number, thermal diffusivity, and pore-scale Reynold number, respectively, in the preceding equations. Utilizing the PCM density, viscosity, and thermal diffusivity, Pr was calculated Pr=$\rho \times \mu/\alpha$ in which $\alpha=(k/(\rho C_p))$,

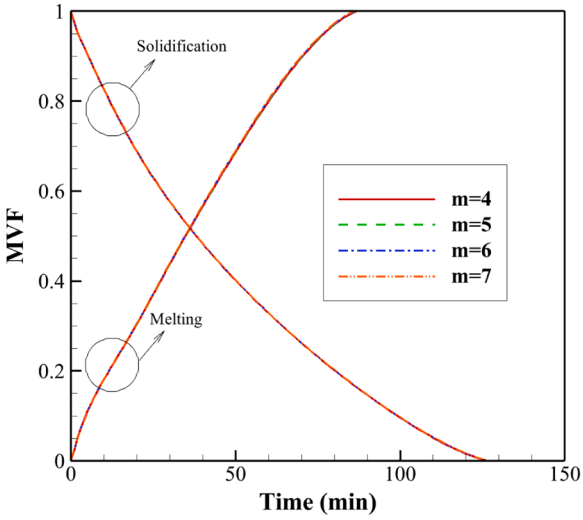

Fig. 5. The impact of mesh resolution parameter (m) on the melting and solidification process.

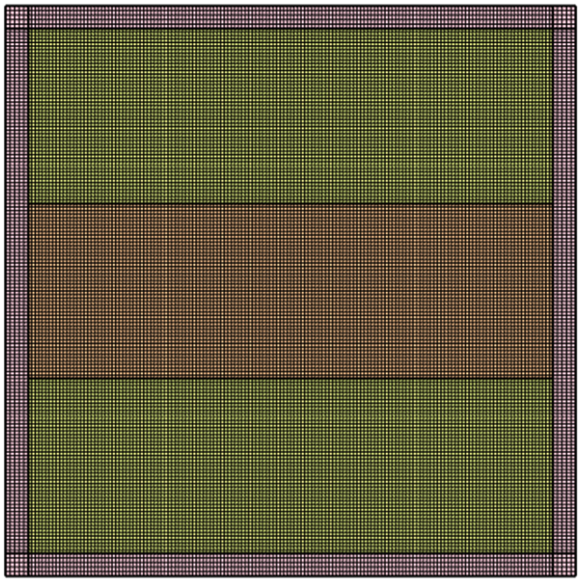

Fig. 6. A view of adopted mesh with m=5.

and all properties are for the PCM. Using the PCM density, velocity, and diameter of the solid PCM region, the pore scale Reynold number was established. Existing research has offered numerous estimation relationships for the Nusselt number. However, these correlations are often applicable for Reynold numbers greater than one. The current study utilizes a relation reported by Yao et al. [30] for the particular range of Re since the circulation velocities of PCM in MF are typically small, and the pore scale Reynold number is smaller than unity. This relationship has been empirically confirmed and is consistent with the phase transition of PCMs in MF. Using the equation stated in sources [41, 44], the PCM's effective thermal conductivity was found. In addition, Eq. (10) is recommended for 21<Pr<41 and 0.929<ε<0.974.

$$k_{\mathrm{eff,\,PCM}} = \frac{2+\varepsilon}{3} k_{\mathrm{PCM}} \quad (11a)$$

As demonstrated in Eq. 11(b) and (c), the thermophysical characteristics of the PCM were calculated from a linear weight average.

$$(\rho C_p)_{\mathrm{PCM}} = (1-\varphi)(\rho C_p)_1 + \varphi(\rho C_p)_s \quad (11b)$$

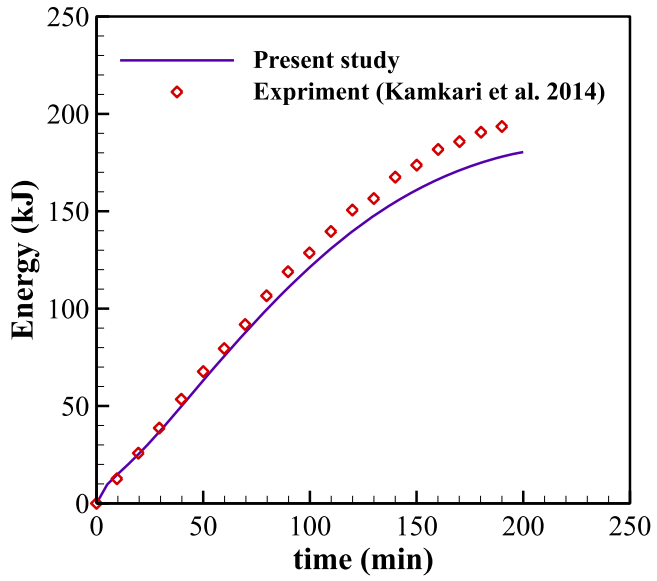

Fig. 7. Comparison of stored energy measurements during the melting process by [59] versus the present simulated data.

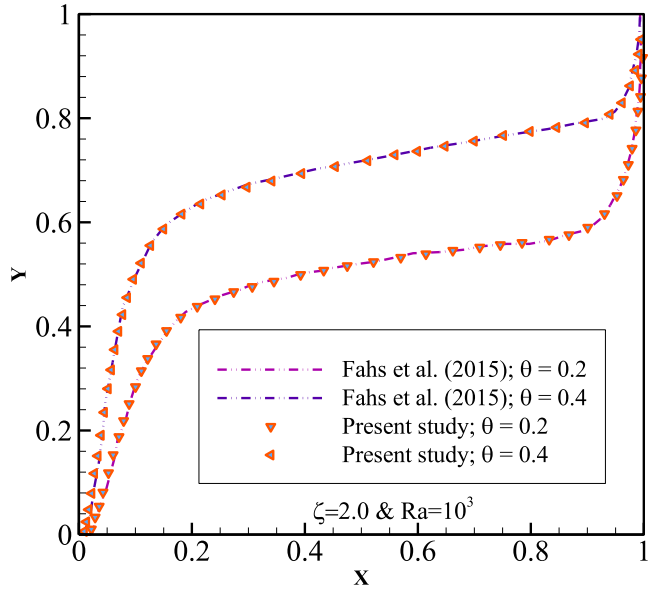

Fig. 8. Influence of anisotropic angle on natural convection heat transfer - a juxtaposition between results from Fahs et al. [61] and our current simulations.

$$\rho_{PCM} = (1-\varphi)\rho_l + \varphi\rho_s \tag{11c}$$

Here, the liquid and solid phases of the PCM are represented by *l* and *s*, respectively. Table 1 provides a summary of the thermophysical parameters of the tube, MF, and paraffin.

Moreover, the melting temperature range of 49-54°C of the PCM and its corresponding enthalpy of fusion ($L = 176$ kJ/kg) were adopted from [48]. The dynamic viscosity and thermal expansion coefficient of the PCM is also adopted as[48-50]: 0.0036 kg/m.s and 0.0009 1/K, respectively. The HTF thermophysical properties were adopted as [52]: dynamic viscosity (μ_f=0.000957 kg/m.s), expansion coefficient (β =0.00021 1/K), density (997.1 kg/m^3), thermal conductivity (0.613 W/m.K), and heat capacity (4179 J/kg.K).

2.2. Initial and boundary conditions

All coupled interfaces were enforced with the exchange of temperature and heat flux. Temperature conservation was imposed on the MF region with LTNE conditions. The heat flux continuity at the conjugate interfaces was defined as follows [16]:

$$q_{Wall} = \varepsilon q_{MF} + (1-\varepsilon) q_{PCM} \tag{12}$$

Eq. (12) explains that the heat from the surface enters the porous matrix and PCM inside the pores proportional to their surface area. The surface area is assumed equal to the foam porosity ε.

A high temperature of T_{wall}=T_f+15°C was assumed for the heated wall. The other enclosure walls were considered to be insulated with -n. q=0, and all wall surfaces were subjected to no-slip and impermeability boundary conditions. The starting temperature of the LHTES unit was assumed to be T_0=T_f-15°C, and a zero-relative-pressure reference point was positioned in the lower left corner of the enclosure. At the interface between the porous layer and the zone of clear flow, temperature and heat flux continuity was preserved. In addition, continuity of velocity and shear stress was applied at the interface between the foam layer and PCM. The metal foam layer temperature at the interface was believed to be equal to that of the PCM. For discharging, the initial temperature is T_0=T_h and T_{wall}=T_c.

Due to the low-temperature variation in the investigation, the thermophysical characteristics were assumed to be constant, with the exception of the PCM properties during phase transition. In addition, the Boussinesq model was used to capture the buoyancy forces in molten PCM.

2.3. Characteristics parameters

The average quantity of melted PCM is represented by the melting volume fraction and can be calculated using the given formula:

$$MVF = \frac{\oint_V \varepsilon\varphi dV}{\oint_V \varepsilon dV} \tag{13}$$

in which the volume element of the shell domain is dV. The total stored thermal energy was calculated by summing the latent and sensible heat:

$$\begin{aligned} Q_{sensible} &= \left[\oint_V \left(\int_{T_0}^{T} \varepsilon(\rho C_P)_{PCM}(T)dT\right)dV\right] \\ &+ (T-T_0)(\rho C_P)_{MF}\oint_V (1-\varepsilon)dV \\ &+ (T-T_0)(\rho C_P)_{Wall}V_{Wall} + (T-T_0)(\rho C_P)_{HTF}V_{HTF} \end{aligned} \tag{14a}$$

$$Q_{latent} = \varepsilon \oint_V \rho_{PCM}\varphi L_{PCM} dV \tag{14b}$$

$$Q_{store} = Q_{latent} + Q_{sensible} \tag{14c}$$

The energy storage power is the amount of stored energy over time as:

$$\text{Power} = Q_{store}/t \tag{14d}$$

The thermal energy storage power is the amount of energy stored between the initial state of the cold PCM to a specific time in the charging process.

3. Quantitative approach and model assessment

This segment outlines the specifics of the quantitative approach, mesh sensitivity analysis, and assessments of the model.

3.1. Employment of the finite element method

The principal equations, together with their initial and boundary

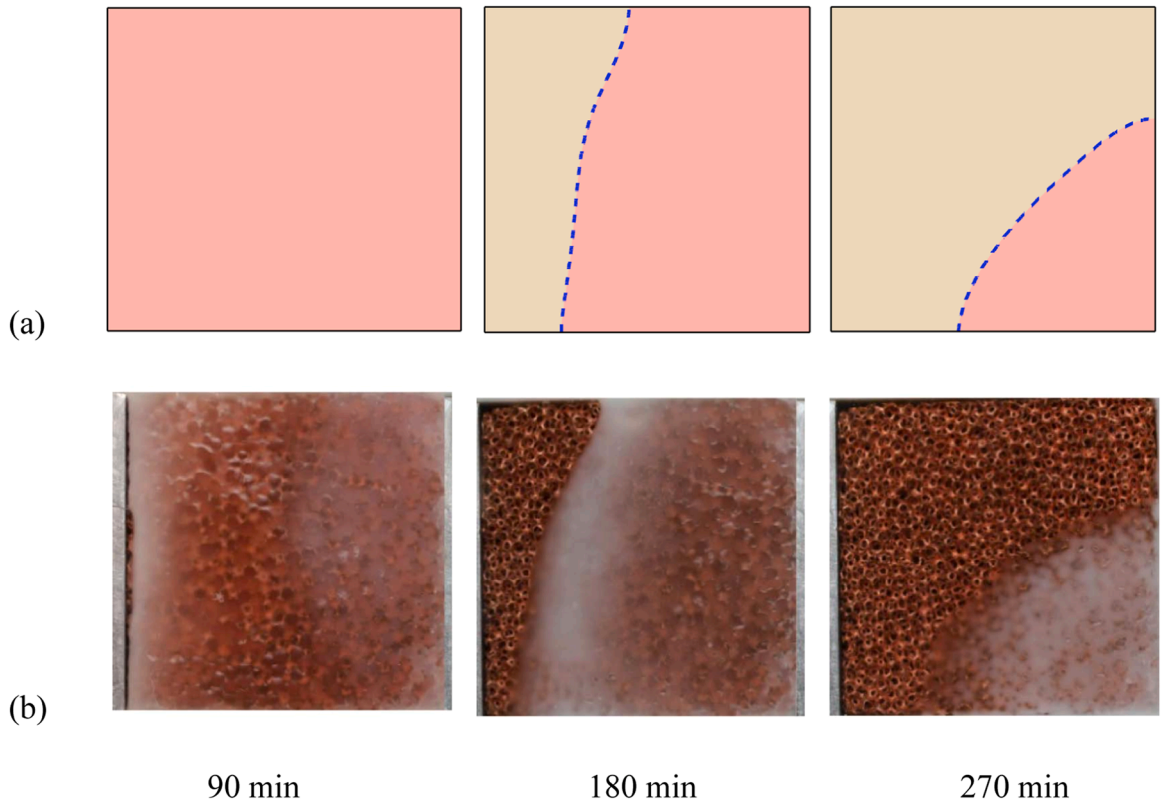

Fig. 9. Melting of hybrid paraffin wax PCM-MF in a square enclosure: (a) findings from our current research and (b) empirical observation [51].

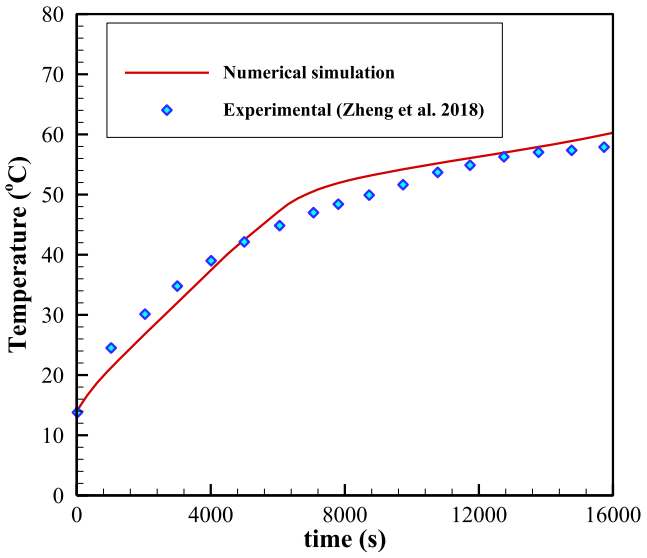

Fig. 10. Verification of current study through comparison with empirical [51] measurements.

parameters, were deciphered utilizing the finite element method (FEM). This technique was utilized to effectively manage the nonlinear sink/source variables arising from phase change [53,54]. By employing a weak form of the principal equations and adopting a second-order partitioning for thermal and momentum equations, a set of algebraic residual equations was derived through element wise Gauss quadrature integration. These equations were solved in an iterative, interconnected way employing the Newton method [55,56], with 0.9 as the damping coefficient to augment convergence. The PARDISO parallel solver, in tandem with the Newton method, was utilized to execute calculations benefiting multiple computational cores in parallel [57,58]. The timing of solution steps and convergence were autonomously adjusted to keep the relative solution precision below 10^{-4}, implementing the first-second order backward differential formula.

The FEM provides a seamless, precise, and even outcome across the partitioned mesh, well-suited for the objectives of the current study. Calculations commenced with the initial conditions and proceeded to examine the energy storage and phase transition behavior. The thermal and continuity equations, together with phase field variable terms (φ), were deemed to be fully integrated and were solved iteratively. The computation was programmed to halt upon the achievement of a fully melted state, indicated by an MVF $\geq$ 0.99 or more, acting as the stopping criteria. A termination criterion of MVF<0.01 was adopted for the solidification process. A diagram illustrating the computational algorithm implemented is presented in Fig. 4.

3.2. Mesh sensitivity analysis

To analyze the effect of mesh resolution on the computational accuracy, a test case, AMFL in the middle, and σ=0.3, γ=0°, was examined during the melting and solidification of PCM. The geometrical values were adopted as: H=150 mm, t_{wall}= 2 mm, and t_1=t_2=t_3. These geometrical details were also used for the results.

A structured mesh discretized the domain of solution. The mesh size was controlled by a mesh resolution parameter m. Table 2 depicts the details of produced meshes and the corresponding computational time for a full melting/solidification process. Fig. 5 depicts the MVF during the melting process for various mesh sizes.

Based on Table 2, a clear and consistent trend of increasing computational requirements is observed as the mesh resolution parameter (m) increases. This trend is unsurprising, given that the number of quadrilateral elements (Quads) and edge elements both increase with higher mesh resolution. For m = 4, there are 16,384 Quads and 1,264 edge elements, requiring approximately 2 h and 57 min for the melting

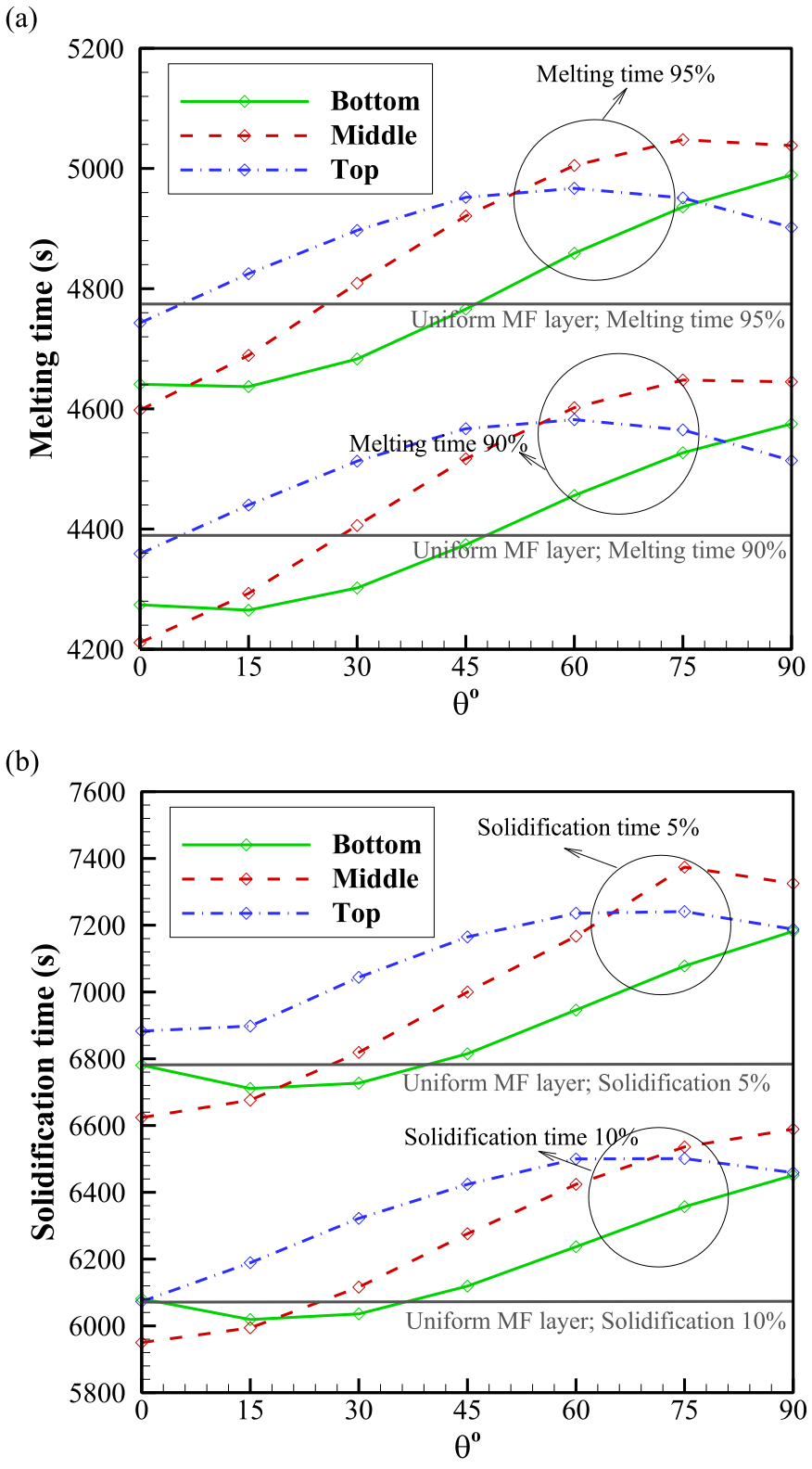

Fig. 11. The required time for melting and solidification: (a) Melting for MVF=0.9 (90 %) and MVF=0.95 (95 %) and solidification for MVF=0.1 (10 %) and MVF=0.05 (5 %). The reference cases for uniform MF layers were also added to the images for the sake of comparisons.

phase and 50 min for the solidification phase. As m increases, the mesh becomes denser, resulting in a higher number of elements to compute. For example, with $m = 5$, the computational time for melting rises to 5 h and 2 min, while the solidification phase lasts 1 h and 19 min. Notably, when $m = 7$, despite a further quantity increase of Quads and edge elements, the computational time for melting does not exhibit the same increment as observed from $m = 5$ to $m = 6$. The reason is due to the use of BDF automatic time-step, which tries to keep the relative accuracy of the solution below 10^{-4}. Thus, this fine mesh size (m=7) could lead to larger time steps and reduce the overall required computational time. Thus, using a fine mesh can have the advantage of solver stability and adopting large time steps. Therefore, in order to ensure computational

Table 3
The charging and discharging times for various anisotropic angles (θ).

Cases	θ °	Melting time 90% (s)	Melting time 95% (s)	Solidification time 10% (s)	Solidification time 5% (s)
MF layer at the top	0	4359	4743	6073	6883
	15	4440	4825	6189	6898
	30	4513	4897	6322	7044
	45	4567	4952	6424	7165
	60	4582	4967	6500	7236
	75	4565	4951	6501	7241
	90	4514	4902	6459	7188
MF layer at the middle	0	4211	4598	5950	6624
	15	4293	4689	5994	6676
	30	4406	4809	6116	6819
	45	4517	4921	6276	7000
	60	4602	5005	6424	7167
	75	4648	5048	6536	7374
	90	4645	5038	6589	7325
MF layer at the bottom	0	4274	4641	6081	6781
	15	4265	4637	6019	6711
	30	4302	4683	6036	6727
	45	4374	4766	6119	6815
	60	4456	4859	6237	6946
	75	4527	4936	6357	7078
	90	4575	4989	6451	7182
Uniform MF layer	-	4390	4774	6081	6781

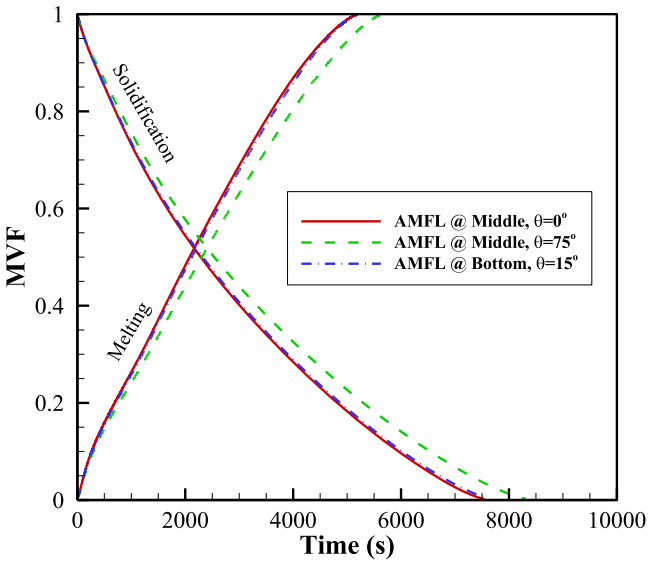

Fig. 12. Time history of selected cases during the melting and solidification processes

Table 4
The stored energy for selected designs: AMFL at Middle θ=0°, AMFL at Middle θ=75°, AMFL at Bottom θ=15°, uniform MF layer (no anisotropic layer).

Case	Anisotropic angle (θ) °	Melting 90 % ΔES (J)	90 % Charging Power (W)	Melting 95 % ΔES (J)	95 % Charging power (W)
1	AMFL at Middle θ=0°	5,744,850	1364	6,021,389	1310
2	AMFL at Middle θ=75°	4,366,218	956	4,567,534	923
3	AMFL at Bottom θ=15°	5,590,517	1302	5,881,433	1254
4	Uniform MF layer	5,594,511	1274	5,885,188	1233

accuracy and solver stability, the mesh of case m=5 was adopted for computations. Fig. 6 provides a view of the adopted mesh with m=5. As seen a uniform structured quadrilateral mesh is utilized in the present study. The structured mesh benefits from uniform quality and shape factors across the domain and can provide high accuracy during the finite element computations. By using the structured mesh, the skewness of the mesh, a critical factor in determining the quality of numerical simulations, is maintained at a minimal level.

3.3. Model verification

Phase change heat transfer with natural convection was simulated under the same conditions as Kamkari et al. [59] to check the accuracy and correctness of the current model and simulations. In [59], the PCM was lauric acid, and the melting proceeded in a cavity with a height of 120 mm and a width of 50 mm. The cavity's left surface was subject to an isothermal heat condition of 70°C and an initial temperature of 25°C. The median of the PCM's fusion temperature was 46°C. The details of the thermophysical properties for lauric acid can be found in Table 1 of [59]. Fig. 7 plots the computed stored energy during the charging process against the reported measured data by [59]. This figure represents a good agreement between data. Moreover, the current model was further compared to the experimental reports of Al-Jethelah et al. [60], who investigated melting heat transfer in metal foams. The results were found very close, which shows the accuracy of the current model and codes. The results were not reported here for conciseness.

Fahs et al. [61] explored the flow of free convection within an anisotropic porous substance possessing a local thermal conductivity contingent on the spatial coordinates of the material. This gradient was contingent on a distribution variable, ζ. When ζ was equivalent to 2.0, the dimensionless temperatures from [61] were juxtaposed with the numerical data from our current research, as portrayed in Fig. 8. The results illustrated in Fig. 8 show a substantial correlation between the current computations and those from previous research.

In terms of the melting process of hybrid paraffin wax PCM-MF, the outcomes from our current software were contrasted with the empirical data presented by Zheng et al. [51]. Paraffin wax was melted in a 100 mm square enclosure where a constant heat flux (1150 W) was applied to a single vertical wall, with minor heat dissipation from the sides of the enclosure. The porosity and PPI of the copper metal foam were 0.95 and 5, respectively. In both studies, the left vertical cavity wall is heated and the other walls are covered by thermal barrier materials. The liquid-solid interface at 90 min, 180 min, and 270 min of melting is depicted in Fig. 9. Fig. 10 also depicts the mean temperature at a vertical line located 2.5 cm away from the heated surface. As seen, the melting interfaces of the present simulation shows close patterns to that of Zheng et al. [51] in Fig. 9. Besides, the results of the present numerical simulation, depicted by the continuous line, shows similar trend and close approximately to the experimental measurements of Zheng et al. [51] in Fig. 10.

4. Results and discussion

The anisotropic parameter for the heterogenous foam layer was considered at a fair value of σ=0.3. The anisotropic angle ($0 \le \theta \le 90$) was investigated for three cases of the AMFL at the top, the middle, or bottom of the cavity. The results were investigated for cases of charging and discharging. The geometric values used in the mesh study section were also applied in this analysis.

The shortest melting/solidification time also corresponds to the middle anisotropic MF layer with zero anisotropic angle. The case with an anisotropic MF layer in the middle with θ=75° shows the longest phase change time for both melting and solidification cases at the final charging times (5 % solidification and 95 % melting). After that, the middle anisotropic MF layer with an anisotropic angle of 90° provides the longest melting and solidification times. Generally, placing the anisotropic MF layer at the bottom provides shorter solidification times

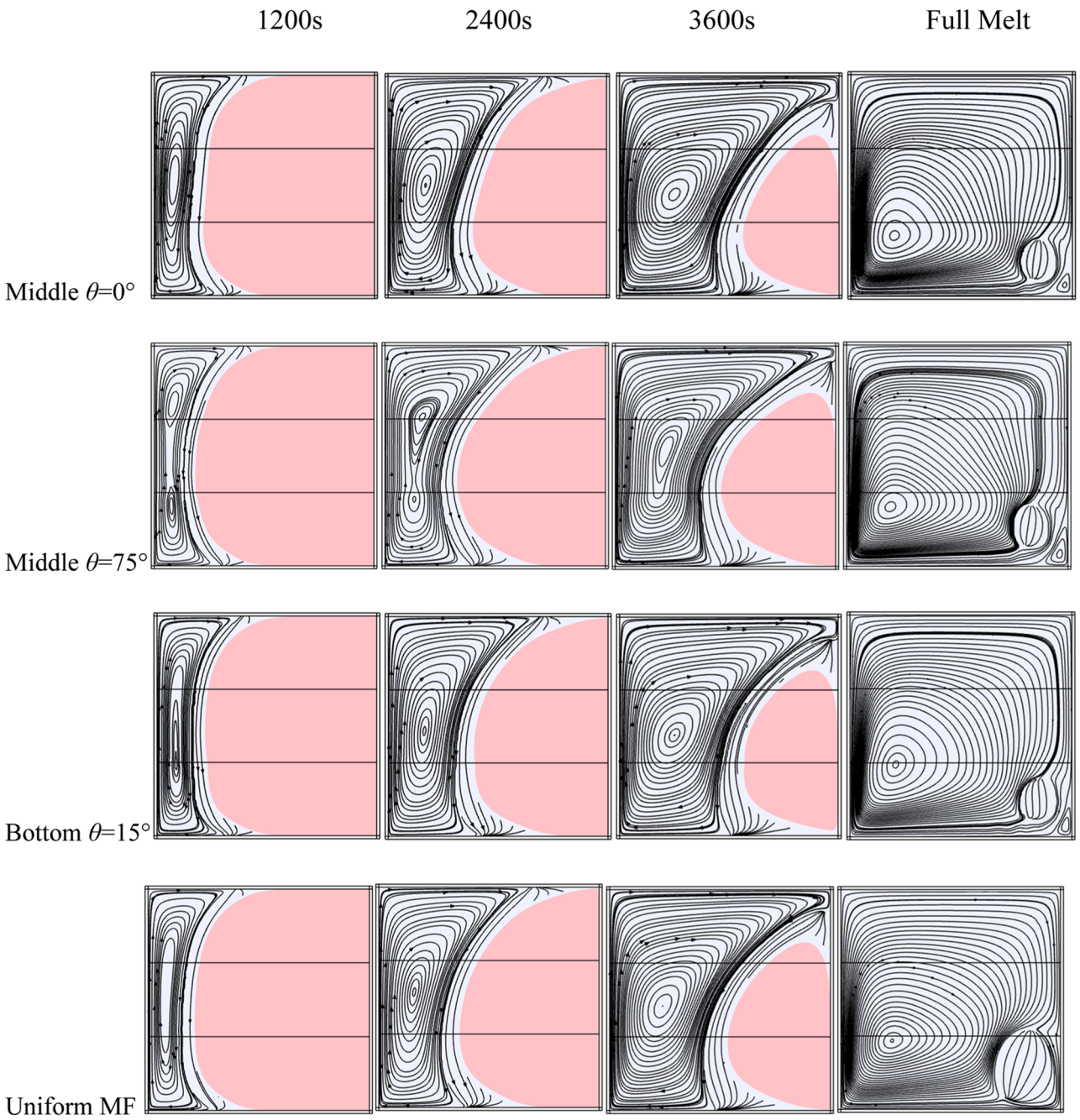

Fig. 13. The melting interface and streamlines for selected designs: AMFL at Middle θ=0°, AMFL at Middle θ=75°, AMFL at Bottom θ=15°, uniform MF layer (no anisotropic layer).

compared to AMFL at the top. AMFL at the bottom also provides a shorter melting time than that of anisotropic ML at the bottom except for θ=90°, in which placing the AMFL at the top could provide a shorter melting time. Attention to the results of Fig. 11 (a) and (b) and Table 3 clarifies that the best design can be obtained for a middle anisotropic ML with an anisotropic angle θ=0°. Considering the mesh study, the accuracy of the computations is about 0.1 %.

Placing the anisotropic MF layer at the bottom with θ=15° would also provide fair melting and solidification results. Thus, the MVF time history for the following interesting cases are plotted in Fig. 12: AMFL at the middle and θ=0° (best design), anisotropic MF layer at the bottom and θ=15° (fair design), anisotropic MF layer at the middle and θ=75° (worst design), and a uniform porous medium design with no anisotropic layers (reference).

To enhance clarity, Fig. 11 has been included to visually represent the results. The reference cases are depicted as straight lines since they do not involve a heterogeneous MF layer, making them independent of anisotropic angles. The use of a well-designed AMFL can lead to shorter melting and solidification times compared to a uniform metal foam. However, an AMFL that is not well designed can impede the melting and solidification process, resulting in increased time to fully melt and solidify the PCM.

For instance, when the AMFL is placed at the bottom with an anisotropic angle θ=15°, the melting time for achieving 95 % melting is 4637 seconds, whereas the uniform case (reference case) reaches 95 % melting in 4774 seconds. Consequently, utilizing the AMFL at the bottom reduces melting time by 2.9 %. Conversely, when using the AMFL at the bottom with θ=90°, the melting time (95 %) increases to 4989 seconds, which is approximately 4.5 % longer than the reference time of 4774 seconds. The best design of the AMFL at the middle with

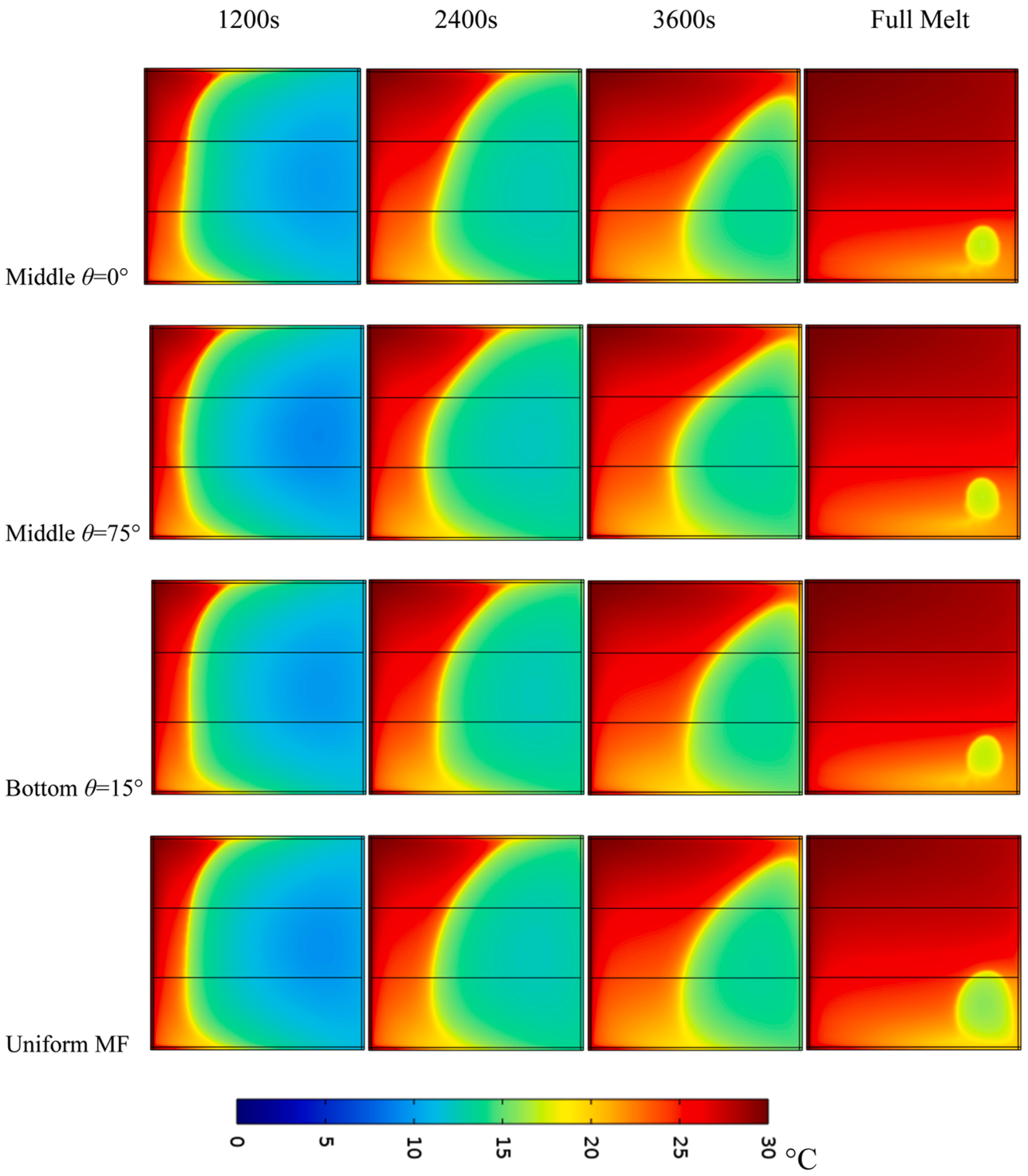

Fig. 14. The temperature contours for selected designs: AMFL at Middle θ=0°, AMFL at Middle θ=75°, AMFL at Bottom θ=15°, uniform MF layer (no anisotropic layer).

θ=0° results in a reduction of roughly 3.7 % in melting time (MVF=0.95) and about 2.3 % in solidification time (MVF=0.05) compared to the reference cases.

In Fig. 12, the time history of melting and solidification is presented for two well-designed cases: AMFL at the middle (θ=0°) and AMFL at the bottom (θ=15°), as well as a not well-designed case of AMFL at the middle (θ=75°). The thermal behavior of melting and solidification in both well-designed cases are nearly identical, especially during the initial stages, where the phase change primarily occurs through conduction heat transfer. However, slight differences between the two cases can be observed during the later stages when natural convection circulations come into play.

When the dominant process of heat transfer is conduction, the placement of the AMFL at the bottom or middle has minimal impact on the heat transfer behavior since the specific location is not significantly important. However, in the case of the not well-designed AMFL in the middle (θ=75°), the rate of phase change gradually decreases as the melting/solidification process progresses. This results from the lower

thermal conductivity perpendicular to the heated surface, where conduction heat transfer should primarily occur. Additionally, the permeability along the heated surface is higher, leading to upward movement of the heated liquid due to natural convection effects. Consequently, utilizing an AMFL with such an anisotropic angle not only fails to provide advantages in heat transfer but also hampers important heat transfer mechanisms such as conduction and convection. The total stored energy and power rate for these investigated cases are computed and reported in Table 4. Remarkably, the maximum 90 % ΔES of 5,744,850 J and 90 % charging power of 1364 W are recorded when AMFL is at the middle with an angle of 0°, which is also the best design case. For the 95 % measurements, the same configuration also gives the highest results. AMFL at the middle (θ=0°) could provide about 7.1 % (for MVF=0.9) and 6.3 % (for MVF=0.95) charging power improvement compared to the reference case.

Figs. 13 and 14 illustrate the progression of the melting interface, temperature contours, and streamlines over four time intervals (the 1200s, 2400s, 3600s, and at complete melting) for the configurations specified in Table 4. Full melting times for AMFL at Middle θ=0°, AMFL at Middle θ=75°, AMFL at Bottom θ=15°, and Uniform MF Layer (no anisotropic layer) were recorded as 5177s, 5629s, 5195s, and 5186s respectively.

Initially, the melting is more prominent in the enclosure's top and bottom, owing to the heat dispersion from the copper walls, which act akin to thermal fins. As time progresses (at t=2400s and t=3600s), natural convection currents stimulate the circulation of molten PCM within the enclosure, further advancing the melting front, especially at the top regions.

However, the AMFL at Middle θ=75° case exhibits a slower melting front at the top due to the lower thermal conductivity in the x-direction and higher permeability in the y-direction at the middle layer. Despite a favorable temperature gradient in the x-direction (Fig. 14), this case's low thermal conductivity hinders the full exploitation of these gradients, thus impeding the melting of PCM. Additionally, the middle layer's low permeability limits upward streamline movement adjacent to the melting interface.

In all scenarios, the final PCM melts at the lower corner of the enclosure as the hot liquid moves upwards before reaching the bottom, resulting in the weakest heat transfer and temperature gradients. Temperature contours show a horizontal gradient in the middle and vertical gradients at the top and bottom.

It can be observed that positioning an AMFL layer in the middle at zero degrees, which provides good conduction in the horizontal direction, can enhance heat transfer by leveraging these temperature gradients. However, if the layer is placed at the top or bottom, other angles might be needed to maximize the heat transfer potential of vertical or mixed temperature gradients. This explains why AMFL at the Bottom θ=15° outperforms the zero-degree configuration for the same layer.

5. Conclusions

Anisotropic metal foams show promising potential to enhance the efficiency of LHTES units thanks to their ability to improve heat transfer and thermal energy storage rates without affecting weight or capacity. However, research into the thermal behavior of these foams across different configurations and enclosure designs is limited. The present study has made strides in filling this knowledge gap by investigating the impact of anisotropic metal foam layer placement and angle on the charging and discharging behavior of an LHTES unit. Here, a LHTES unit with a channel configuration was investigated. The channels were constructed using copper, filled with three layers of copper metal foam, one of which is an anisotropic layer infused with paraffin wax. The FEM was used to solve the governing equations and manage the nonlinearities arising from phase change. Both solidification and melting cases were simulated for the anisotropic angle between 0-90°. Furthermore, three different placements of the AMFL were studied: top, middle, or bottom of the enclosure. The main findings can be listed as flows:

- The simulations showed that the fastest melting/solidification time corresponded to the middle placement of the AMFL with zero degrees anisotropic angle. Conversely, the longest phase change time was observed for the middle placement with a 75° anisotropic angle.
- The best design case can be obtained for a middle AMFL with an anisotropic angle of zero degrees. This configuration resulted in an approximately 3.7 % reduction in melting time and about 2.3 % reduction in solidification time compared to the reference cases. Another fair performing design had the AMFL at the bottom with a 15° anisotropic angle.
- Poorly designed AMFLs, like those with a middle placement and a 75° anisotropic angle, were shown to impede the melting and solidification process. This potentially increased the charging (melting) and discharging (solidification) times. The study suggests that the placement and angle of the AMFL layer play a significant role in the heat transfer and energy storage performance of LHTES units.
- The placement of the AMFL in the middle at zero degrees was found to leverage temperature gradients optimally, thus enhancing heat transfer. In contrast, positioning at the top or bottom might require other angles to maximize heat transfer potential due to vertical or mixed temperature gradients. Interestingly, the maximum 90 % ΔES of 5,744,850 J and 90 % charging power of 1364 W were achieved with an AMFL in the middle with a 0°. It offers an improvement of approximately 7.1 % for MVF=0.9 and a substantial 6.3 % for MVF=0.95 when contrasted with the reference case, thus confirming its superiority for efficient thermal energy storage.

CRediT authorship contribution statement

Mohammad Ghalambaz: Validation, Supervision, Software, Methodology, Formal analysis, Data curation, Conceptualization. **Mikhail Sheremet:** Writing – original draft, Visualization, Supervision, Investigation, Formal analysis, Data curation. **Kyle Shank:** Writing – original draft, Visualization, Investigation, Formal analysis, Data curation. **Saeed Tiari:** Writing – original draft, Supervision, Investigation, Formal analysis. **Mehdi Fteiti:** Writing – review & editing, Software, Methodology, Investigation, Formal analysis, Data curation.

Declaration of competing interest

The authors clarify that there is no conflict of interest for report.

Data availability

No data was used for the research described in the article.

Acknowledgments

The authors would like to thank the Deanship of Scientific Research at Umm Al-Qura University for supporting this work by Grant Code: (23UQU4310414DSR012). This research of Mikhail Sheremet and Mohammad Ghalambaz was supported by the Tomsk State University Development Programme (Priority-2030).

References

[1] S.C. Costa, M. Kenisarin, A review of metallic materials for latent heat thermal energy storage: thermophysical properties, applications, and challenges, Renew. Sustain. Energy Rev. 154 (2022) 111812.
[2] P. Gadhave, F. Pathan, S. Kore, C. Prabhune, Comprehensive review of phase change material based latent heat thermal energy storage system, Int. J. Ambient Energy 43 (1) (2022) 4181–4206.
[3] C. Zeng, Y. Yuan, F. Haghighat, K. Panchabikesan, M.M. Joybari, X. Cao, L. Klimeš, Application of PCM-based thermal energy storage system in buildings: a state of the

art review on the mathematical modeling approaches and experimental investigations, J. Therm. Sci. 31 (6) (2022) 1821–1852.
[4] P.K.S. Rathore, S.K. Shukla, Enhanced thermophysical properties of organic PCM through shape stabilization for thermal energy storage in buildings: a state of the art review, Energy Build. 236 (2021) 110799.
[5] A. Agrawal, D. Rakshit, Review on thermal performance enhancement techniques of latent heat thermal energy storage (LHTES) system for solar and waste heat recovery applications, New Res. Dir. Sol. Energy Technol. (2021) 411–438.
[6] P. Arumugam, V. Ramalingam, P. Vellaichamy, Effective PCM, insulation, natural and/or night ventilation techniques to enhance the thermal performance of buildings located in various climates–a review, Energy Build. (2022) 111840.
[7] X. Wang, W. Li, Z. Luo, K. Wang, S.P. Shah, A critical review on phase change materials (PCM) for sustainable and energy efficient building: design, characteristic, performance and application, Energy Build. 260 (2022) 111923.
[8] K. Du, J. Calautit, P. Eames, Y. Wu, A state-of-the-art review of the application of phase change materials (PCM) in mobilized-thermal energy storage (M-TES) for recovering low-temperature industrial waste heat (IWH) for distributed heat supply, Renew. Energy 168 (2021) 1040–1057.
[9] B. Purohit, V. Sistla, Inorganic salt hydrate for thermal energy storage application: a review, Energy Storage 3 (2) (2021) e212.
[10] M. Eslami, F. Khosravi, H.F. Kohan, Effects of fin parameters on performance of latent heat thermal energy storage systems: a comprehensive review, Sustain. Energy Technol. Assess. 47 (2021) 101449.
[11] F. Ma, T. Zhu, Y. Zhang, X. Lu, W. Zhang, F. Ma, A review on heat transfer enhancement of phase change materials using fin tubes, Energies 16 (1) (2023) 545 (Basel).
[12] J. Shi, H. Du, Z. Chen, S. Lei, Review of phase change heat transfer enhancement by metal foam, Appl. Therm. Eng. (2022) 119427.
[13] M. Aramesh, B. Shabani, Metal foams application to enhance the thermal performance of phase change materials: a review of experimental studies to understand the mechanisms, J. Energy Storage 50 (2022) 104650.
[14] T. Tayebi, A.J. Chamkha, H.F. Öztop, L. Bouzeroura, Local thermal non-equilibrium (LTNE) effects on thermal-free convection in a nanofluid-saturated horizontal elliptical non-Darcian porous annulus, Math. Comput. Simul. 194 (2022) 124–140.
[15] T. Tayebi, A.J. Chamkha, Analysis of the effects of local thermal non-equilibrium (LTNE) on thermo-natural convection in an elliptical annular space separated by a nanofluid-saturated porous sleeve, Int. Commun. Heat Mass Transf. 129 (2021) 105725.
[16] D.A. Nield, A. Bejan, Convection in Porous Media, 5th ed., Springer, 2017.
[17] N.B. Khedher, J.M. Mahdi, H.S. Majdi, W.K. Al-Azzawi, S. Dhahbi, P. Talebizadehsardari, A hybrid solidification enhancement in a latent-heat storage system with nanoparticles, porous foam, and fin-aided foam strips, J. Energy Storage 56 (2022) 106070.
[18] X. Li, J. Duan, T. Simon, T. Ma, T. Cui, Q. Wang, Nonuniform metal foam design and pore-scale analysis of a tilted composite phase change material system for photovoltaics thermal management, Appl. Energy 298 (2021) 117203.
[19] J.M. Mahdi, F.T. Najim, I.M. Aljubury, H.I. Mohammed, N.B. Khedher, N. K. Alshammari, A. Cairns, P. Talebizadehsardari, Intensifying the thermal response of PCM via fin-assisted foam strips in the shell-and-tube heat storage system, J. Energy Storage 45 (2022) 103733.
[20] M.M. El Idi, M. Karkri, Heating and cooling conditions effects on the kinetic of phase change of PCM embedded in metal foam, Case Stud. Therm. Eng. 21 (2020) 100716.
[21] M.A. Alnakeeb, M.M. Sorour, A.O. Alkadi, A.A. Gomaa, A.M. ELghoul, M. M. Zaytoun, The influence of elliptic aspect ratio and inclination angle on the melting characteristic of phase change material in concentric cylindrical enclosure, J. Energy Storage 62 (2023) 106832.
[22] W. Tian, S. Dang, G. Liu, Z. Guo, X. Yang, Thermal transport in phase change materials embedded in metal foam: evaluation on inclination configuration, J. Energy Storage 33 (2021) 102166.
[23] X. Yang, X. Wang, Z. Liu, Z. Guo, L. Jin, C. Yang, Influence of aspect ratios for a tilted cavity on the melting heat transfer of phase change materials embedded in metal foam, Int. Commun. Heat and Mass Transf. 122 (2021) 105127.
[24] Y. Zhuang, Z. Liu, W. Xu, Effects of gradient porous metal foam on the melting performance and energy storage of composite phase change materials subjected to an internal heater: a numerical study and PIV experimental validation, Int. J. Heat. Mass Transf. 183 (2022) 122081.
[25] P. Zhang, Z. Meng, H. Zhu, Y. Wang, S. Peng, Melting heat transfer characteristics of a composite phase change material fabricated by paraffin and metal foam, Appl. Energy 185 (2017) 1971–1983.
[26] Y. Zhao, C. Zhao, Z. Xu, H. Xu, Modeling metal foam enhanced phase change heat transfer in thermal energy storage by using phase field method, Int. J. Heat. Mass Transf. 99 (2016) 170–181.
[27] P. Srivatsa, R. Baby, C. Balaji, Numerical investigation of PCM based heat sinks with embedded metal foam/crossed plate fins, Numer. Heat Transf. Part A Appl. 66 (10) (2014) 1131–1153.
[28] F. Zhu, C. Zhang, X. Gong, Numerical analysis and comparison of the thermal performance enhancement methods for metal foam/phase change material composite, Appl. Therm. Eng. 109 (2016) 373–383.
[29] F. Zhu, C. Zhang, X. Gong, Numerical analysis on the energy storage efficiency of phase change material embedded in finned metal foam with graded porosity, Appl. Therm. Eng. 123 (2017) 256–265.
[30] Y. Yao, H. Wu, Z. Liu, Direct simulation of interstitial heat transfer coefficient between paraffin and high porosity open-cell metal foam, J. Heat. Transf. 140 (3) (2018) 032601.
[31] H.A. Ahmadi, N. Variji, A. Kaabinejadian, M. Moghimi, M. Siavashi, Optimal design and sensitivity analysis of energy storage for concentrated solar power plants using phase change material by gradient metal foams, J. Energy Storage 35 (2021) 102233.
[32] G. Liu, T. Xiao, J. Guo, P. Wei, X. Yang, K. Hooman, Melting and solidification of phase change materials in metal foam filled thermal energy storage tank: evaluation on gradient in pore structure, Appl. Therm. Eng. 212 (2022) 118564.
[33] X. Yang, P. Wei, G. Liu, Q. Bai, Y.L. He, Performance evaluation on the gradient design of pore parameters for metal foam and pin fin-metal foam hybrid structure, Appl. Therm. Eng. 175 (2020) 115416.
[34] C. Yang, Y. Xu, X. Cai, Z.J. Zheng, Melting behavior of the latent heat thermal energy storage unit with fins and graded metal foam, Appl. Therm. Eng. 198 (2021) 117462.
[35] M. Iasiello, N. Bianco, W.K. Chiu, V. Naso, Anisotropic convective heat transfer in open-cell metal foams: assessment and correlations, Int. J. Heat. Mass Transf. 154 (2020) 119682.
[36] P. Yu, Y. Wang, R. Ji, H. Wang, J. Bai, Pore-scale numerical study of flow characteristics in anisotropic metal foam with actual skeleton structure, Int. Commun. Heat Mass Transf. 126 (2021) 105401.
[37] T. Xiao, Z. Du, L. Lu, Y. Li, X. Huang, X. Yang, Y.L. He, Melting of phase change materials inside metal foams with uniform/graded porosity: pore-scale simulation, Appl. Therm. Eng. 232 (2023) 121082.
[38] J. Shafi, M. Ghalambaz, M. Fteiti, M. Ismael, M. Ghalambaz, Computational modeling of latent heat thermal energy storage in a shell-tube unit: using neural networks and anisotropic metal foam, Mathematics 10 (24) (2022) 4774.
[39] M. Ghalambaz, M. Aljaghtham, A.J. Chamkha, A. Abdullah, A. Alshehri, M. Ghalambaz, Anisotropic metal foam design for improved latent heat thermal energy storage in a tilted enclosure, Int. J. Mech. Sci. 238 (2023) 107830.
[40] M. Ghalambaz, M. Aljaghtham, A.J. Chamkha, A. Abdullah, I. Mansir, M. Ghalambaz, Mathematical modeling of heterogeneous metal foams for phase-change heat transfer enhancement of latent heat thermal energy storage units, Appl. Math. Model. 115 (2023) 398–413.
[41] S. Zhang, Y. Yao, Y. Jin, Z. Shang, Y. Yan, Heat transfer characteristics of ceramic foam/molten salt composite phase change material (CPCM) for medium-temperature thermal energy storage, Int. J. Heat. Mass Transf. 196 (2022) 123262.
[42] M. Ghalambaz, A.A. Melaibari, A.J. Chamkha, O. Younis, M. Sheremet, Phase change heat transfer and energy storage in a wavy-tube thermal storage unit filled with a nano-enhanced phase change material and metal foams, J. Energy Storage 54 (2022) 105277.
[43] D.A. Nield, A. Bejan, Convection in Porous Media, Springer, 2006.
[44] Y. Yao, H. Wu, Interfacial heat transfer in metal foam porous media (MFPM) under steady thermal conduction condition and extension of Lemlich foam conductivity theory, Int. J. Heat. Mass Transf. 169 (2021) 120974.
[45] C. Zhao, J. Wang, Y. Sun, S. He, K. Hooman, Fin design optimization to enhance PCM melting rate inside a rectangular enclosure, Appl. Energy 321 (2022) 119368.
[46] M. Ghalambaz, M. Aljaghtham, A.J. Chamkha, A. Abdullah, A. Alshehri, M. Ghalambaz, An anisotropic metal foam design for improved latent heat thermal energy storage in a tilted enclosure, Int. J. Mech. Sci. (2022) 107830.
[47] Y. Yao, H. Wu, Macroscale modeling of solid–liquid phase change in metal foam/paraffin composite: effects of paraffin density treatment, thermal dispersion, and interstitial heat transfer, J. Therm. Sci. Eng. Appl. 13 (4) (2021).
[48] A.I.N. Korti, H. Guellil, Experimental study of the effect of inclination angle on the paraffin melting process in a square cavity, J. Energy Storage 32 (2020) 101726.
[49] A. Agarwal, R. Sarviya, Characterization of commercial grade paraffin wax as latent heat storage material for solar dryers, Mater. Today Proc. 4 (2) (2017) 779–789.
[50] N. Ukrainczyk, S. Kurajica, J. Šipušić, Thermophysical comparison of five commercial paraffin waxes as latent heat storage materials, Chem. Biochem. Eng. Q. 24 (2) (2010) 129–137.
[51] H. Zheng, C. Wang, Q. Liu, Z. Tian, X. Fan, Thermal performance of copper foam/paraffin composite phase change material, Energy Convers. Manage 157 (2018) 372–381.
[52] S.K. Choi, S.O. Kim, T.H. Lee, Dohee-Hahn, Computation of the natural convection of nanofluid in a square cavity with homogeneous and nonhomogeneous models, Numer. Heat Transf. Part A Appl. 65 (4) (2014) 287–301.
[53] O.C. Zienkiewicz, R.L. Taylor, P. Nithiarasu, The Finite Element Method for Fluid Dynamics, 7th ed., Butterworth-Heinemann, Oxford, 2014.
[54] D. Pepper, The Intermediate Finite Element Method: Fluid Flow and Heat Transfer Applications, Routledge, 2017.
[55] C.T. Kelley, Solving Nonlinear Equations with Newton's Method, SIAM, 2003.
[56] P. Deuflhard, Newton Methods for Nonlinear Problems: Affine Invariance and Adaptive Algorithms, Springer Science & Business Media, 2005.
[57] M. Bollhöfer, O. Schenk, R. Janalik, S. Hamm, K. Gullapalli, State-of-the-art sparse direct solvers, Parallel algorithms in computational science and engineering, (2020) 3-33.
[58] M. Bollhöfer, A. Eftekhari, S. Scheidegger, O. Schenk, Large-scale sparse inverse covariance matrix estimation, SIAM J. Sci. Comput. 41 (1) (2019) A380–A401.
[59] B. Kamkari, H. Shokouhmand, F. Bruno, Experimental investigation of the effect of inclination angle on convection-driven melting of phase change material in a rectangular enclosure, Int. J. Heat. Mass Transf. 72 (2014) 186–200.
[60] M. Al-Jethelah, S. Ebadi, K. Venkateshwar, S.H. Tasnim, S. Mahmud, A. Dutta, Charging nanoparticle enhanced bio-based PCM in open cell metallic foams: an experimental investigation, Appl. Therm. Eng. 148 (2019) 1029–1042.
[61] M. Fahs, A. Younes, A. Makradi, A reference benchmark solution for free convection in a square cavity filled with a heterogeneous porous medium, Numer. Heat Transf. Part B Fundam. 67 (5) (2015) 437–462.